Drift-wave transport in the velocity shear layer

K. C. Rosalem, M. Roberto, and I. L. Caldas

Citation: Physics of Plasmas **23**, 072504 (2016); doi: 10.1063/1.4955321
View online: http://dx.doi.org/10.1063/1.4955321
View Table of Contents: http://aip.scitation.org/toc/php/23/7
Published by the American Institute of Physics

Drift-wave transport in the velocity shear layer

K. C. Rosalem,[1] M. Roberto,[1] and I. L. Caldas[2]
[1]Departamento de Física, Instituto Tecnológico de Aeronáutica, São José dos Campos, SP 12228-900, Brazil
[2]Instituto de Física, Universidade de São Paulo, São Paulo, SP 05315-970, Brazil

(Received 29 May 2016; accepted 16 June 2016; published online 12 July 2016)

Particle drift driven by electrostatic wave fluctuations is numerically computed to describe the transport in a gradient velocity layer at the tokamak plasma edge. We consider an equilibrium plasma in large aspect ratio approximation with $\boldsymbol{E}\times\boldsymbol{B}$ flow and specified toroidal plasma velocity, electric field, and magnetic field profiles. A symplectic map, previously derived for infinite coherent time modes, is used to describe the transport dependence on the electric, magnetic, and plasma velocity shears. We also show that resonant perturbations and their correspondent islands in the Poincaré maps are much affected by the toroidal velocity profiles. Moreover, shearless transport barriers, identified by extremum values of the perturbed rotation number profiles of the invariant curves, allow chaotic trajectories trapped into the plasma. We investigate the influence of the toroidal plasma velocity profile on these shearless transport barriers. *Published by AIP Publishing.*
[http://dx.doi.org/10.1063/1.4955321]

I. INTRODUCTION

Tokamak plasma confinement is limited by the electrostatic turbulence and the associated particle transport at the plasma edge.[1,2] The turbulence-driven particle transport is mainly caused by the particle $\boldsymbol{E}\times\boldsymbol{B}$ drift[3–5] at the plasma edge, and the fluctuating electrostatic field is associated with drift waves, driven by equilibrium radial gradients, propagating in the poloidal and toroidal directions.[6] Several experiments in tokamaks show this transport reduced by properly changing the equilibrium radial profiles of the electric and magnetic fields.[7–9]

To investigate the influence of the electric and magnetic fields profiles on the particle transport at the tokamak plasma edge, a guiding-center model was proposed to describe the particle transport, driven by drift waves propagating in the plasma edge, for large aspect ratio tokamaks with an equilibrium $\boldsymbol{E}\times\boldsymbol{B}$ poloidal flow.[10,11] This model has been applied to numerically investigate the onset of transport barriers in tokamaks.[12,13] Complementary, influence of the $\boldsymbol{E}\times\boldsymbol{B}$ poloidal flow on the turbulence and plasma edge transport has been experimentally identified[3,4] and theoretically investigated.[14]

The model introduced in Ref. 11 was used to derive, for a spectrum with infinite coherent time modes, a non integrable symplectic map that describes test particle transport in sheared plasmas. This drift map has been used to numerically investigate the transport dependence on electric and magnetic shears spatial profiles.[13] On the other hand, tokamak experiments and initial simulations show that particle transport depends on the particle velocity profile.[15–18] However, the influence of the velocity profile on the particle transport has not yet been much explored in the mentioned drift map.

In this work, we apply the drift map derived in Ref. 11 to numerically obtain Poincaré maps which show the influence of particle toroidal velocity profile on the particle transport at the plasma edge. In particular, assuming equilibrium profiles for electric and magnetic fields, and plasma flow, we give examples of changes in the shearless invariant lines, observed at the radial position where the rotation number profiles have an extremum. These shearless lines act as internal particle transport barriers separating trajectories in the phase space. Considering a non-monotonic radial electric field profile, for both the monotonic and non-monotonic safety factor profiles, we give examples of the influence of the uniform and non-uniform velocity profiles on the transport and the periodic structures seen in these maps.

In Section II, we present the symplectic map that describes the particle trajectories. In Section III, we introduce the equilibrium electric field, safety factor, and parallel velocity profiles. In Section IV, the parallel velocity effects are investigated for a monotonic safety factor profile. In Section V, we analyze such effects for a safety factor non-monotonic profile and show how the particle transport increases with the potential amplitude. The conclusions are left to the Section VI.

II. DRIFT MAP

The considered plasma configuration corresponds to a layer of a large aspect ratio tokamak. In the considered model, particle trajectories are described by the guiding-center equation of motion

$$\frac{d\boldsymbol{x}}{dt} = v_{\parallel}\frac{\boldsymbol{B}}{B} + \frac{\boldsymbol{E}\times\boldsymbol{B}}{B^2}, \tag{1}$$

where $\boldsymbol{x} = (r, \vartheta, \varphi)$ is written in local polar coordinates with r as the radial position, ϑ and φ, respectively, as the poloidal and toroidal angles. The electric field is composed by a fluctuating component $\tilde{\boldsymbol{E}} = -\nabla\tilde{\phi}$ plus an equilibrium radial field $\boldsymbol{E}_r$, and the magnetic configuration is introduced by the safety factor profile for $B \approx B_{\varphi} \gg B_{\vartheta}$. Here, $v_{\parallel}$ is the particle velocity along to the toroidal direction. In this approximation, the safety factor can be calculated as $\mathrm{q} = rB_{\varphi}/RB_{\vartheta}$.

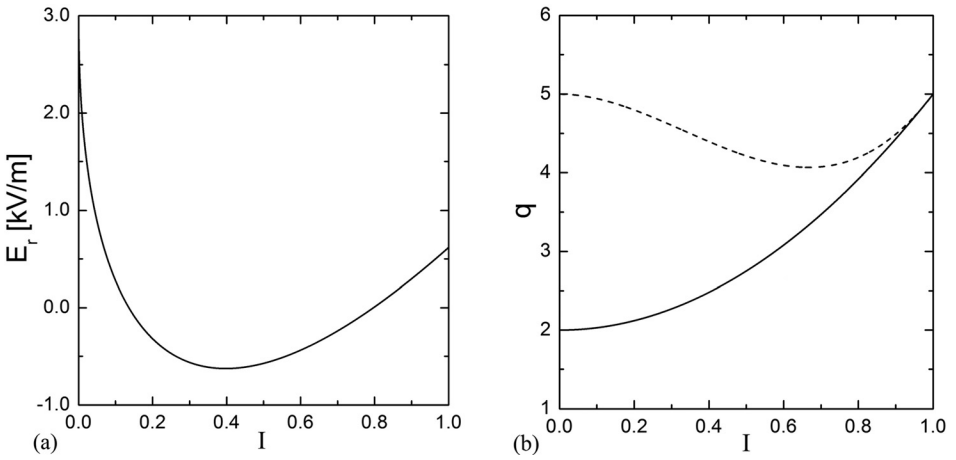

FIG. 1. Radial electric field (a) and safety factor (b) with monotonic profile (solid line) and non-monotonic profile (dashed line).

For the fluctuating potential, we use the finite mode drift wave spectrum,

$$\tilde{\phi}(\boldsymbol{x},t)=\sum_{M,L,n}\phi_{m,l,n}\cos\left(M\vartheta-L\varphi-n\omega_0 t\right), \tag{2}$$

where all mode amplitudes $\phi_{M,L,n}$ are equal for the considered range of radial position, M and L define the dominant spatial modes in this coordinate system, and ω_0 defines the lowest angular frequency with substantial amplitude in the drift wave spectrum. Considering an infinite number of modes with frequencies $n\omega_0$, it is possible to introduce impulsive iterations at $t=2\pi n/\omega_0$.

For convenience, we assume action and helical angle variables,[11] such as $I=(r/a)^2$ and $\Psi=(M\vartheta-L\varphi)$, respectively. In Ref. 11, for the considered wave modes, the following symplectic drift map equations were derived:

$$I_{N+1}=I_N+\frac{4\pi M}{a^2 B\,\omega_0}\phi_{ML}\sin(\chi), \tag{3}$$

$$\chi_{N+1}=\chi_N+R_1(I_{N+1})+R_2(I_{N+1}), \tag{4}$$

$$R_1(I)=\frac{v_{\parallel}(I)}{\omega_0 R\,q(I)}\left[M-L\,q(I)\right], \tag{5}$$

$$R_2(I)=-\frac{M}{\omega_0 a B}\frac{E_r(I)}{\sqrt{I}}, \tag{6}$$

where $\chi=\Psi/2\pi$. To solve these equations, we have to introduce the electric and magnetic equilibrium fields. Furthermore, the parallel velocity profile $v_{\parallel}(I)$ can be inserted in this model considering its experimental dependence with the radial plasma position.[19] Since we are interested in studying what occurs near the plasma edge where $R_1(I)\gg R_2(I)$, the resonance conditions of interest are mainly determined by the safety factor and the parallel velocity profile that appears in $R_1(I)$.

For $\phi_{ML}=0$, the map is integrable, and all orbits are regular, either periodic or quasi-periodic for any initial condition, $I=I_0$ and $\Delta\chi\equiv R_1(I)+R_2(I)$. In this case, the rotation number $\Omega(I)$ is a constant along to the orbit for each initial action I_0. Then, each invariant line is horizontal in the phase space and characterized by its rotation number. The wave inclusion , $\phi_{ML}\neq 0$, breaks the integrability, and I_0 is not anymore a constant of motion. Even so, for the rippled invariant lines, we can define the rotation number as the limit $\Omega=\lim_{i\to\infty}\Delta\Psi_i/i$. Thus, in general, the rotation number $\Omega(I)$ depends on the I value.

On the other hand, considering the wave perturbation, the map describes a mixed phase space with regular and chaotic orbits. The particle transport occurs whenever the orbits are chaotic, and for these orbits, the rotation number is not defined. In this context, the remaining invariant curve acts as transport barriers, but, in general, they can be destroyed by increasing the perturbing wave amplitude.[20] However, an invariant line may resist to be broken if their rotation number is an extremum. This shearless line acts as lasting internal transport barrier,[21] limiting the transport to each side of phase space, and a strength perturbation amplitude is required to break it allowing a global transport.

III. ELECTRIC, MAGNETIC, AND VELOCITY PROFILES

In this work, we assume a spatial dominant mode $M/L=15/6$ and a non-monotonic radial electric field E_r to investigate the influence of $v_{\parallel}$ profiles for monotonic and non-monotonic magnetic configurations given by the safety

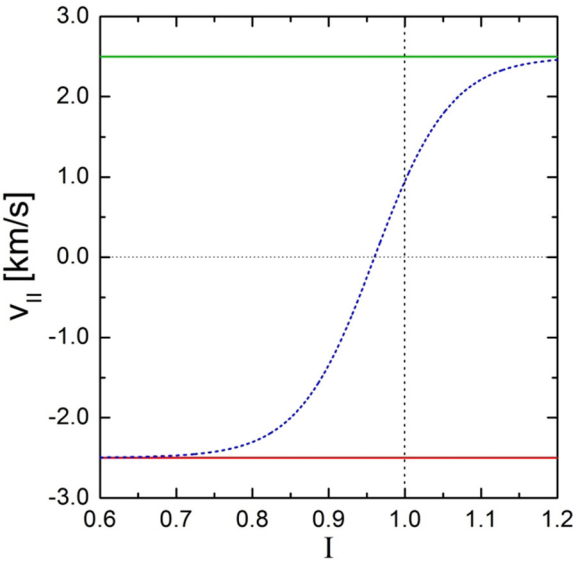

FIG. 2. Radial velocities for positive uniform profile (green line), negative uniform profile (red line), and sheared profile (blue dashed line) at the plasma edge.

factor profiles. For that, particle parallel velocity with positive uniform, negative uniform, and sheared profiles is combined with both magnetic configurations. The parameters and profiles used in the present work are compatible with those chosen in Ref. 19 to simulate the transport in TCABR tokamak.

The non-monotonic electric field profile is given by the expression $E_r = 3\alpha r^2 + 2\beta r + \gamma$, where the coefficients are

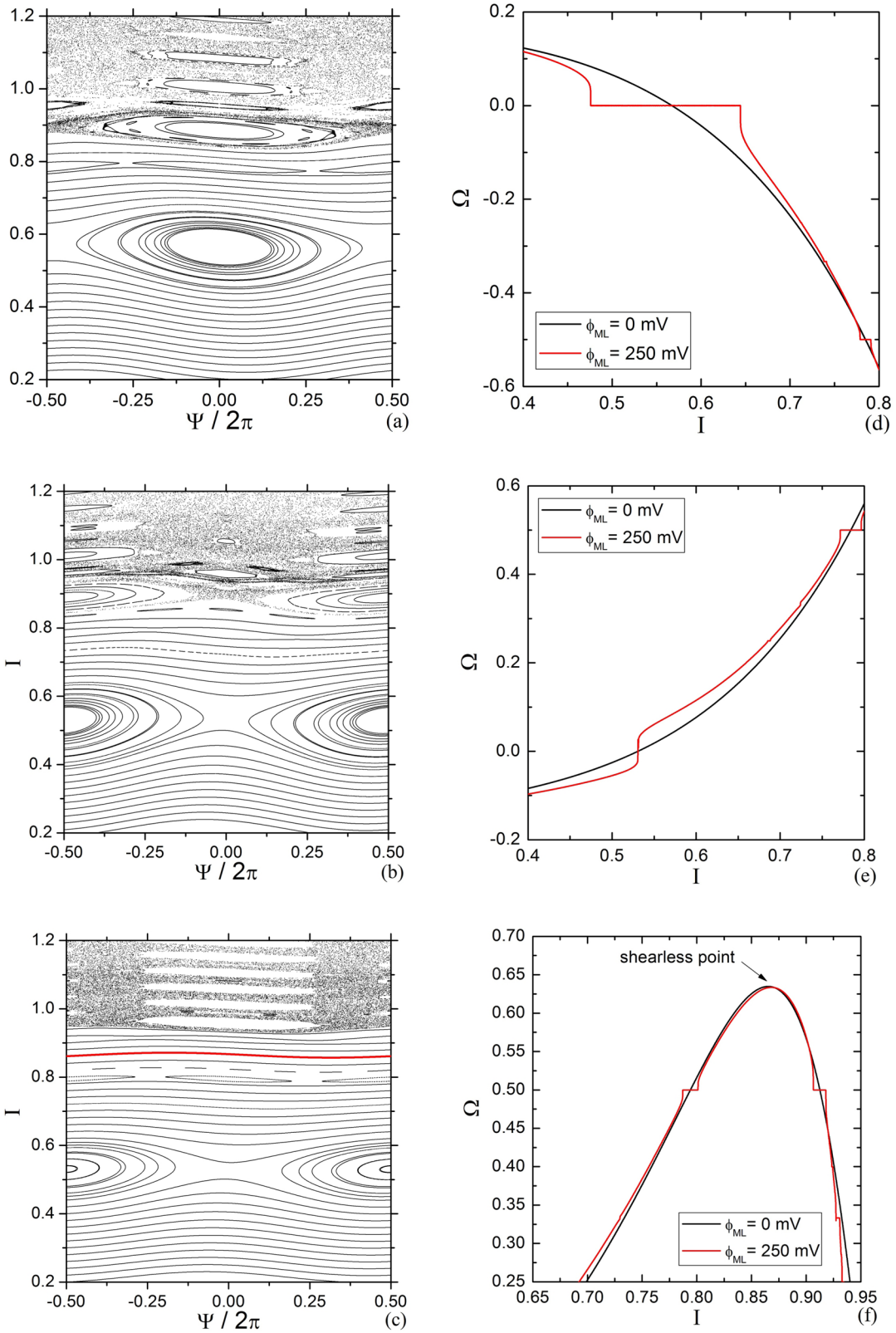

FIG. 3. Poincaré maps for potential mode amplitude $\phi_{ML} = 250\,\text{mV}$ and positive uniform velocity (a), negative uniform velocity (b), and sheared velocity (c) profiles showed in Fig. 2. The shearless curve is depicted in red in (c). For these maps, we used a monotonic safety factor profile showed in Fig. 1(b). Rotation number profiles at $\Psi/2\pi = 0$ for positive uniform velocity (d), negative uniform velocity (e), and sheared velocity (f).

$\alpha = 80.00 \times 10^3$, $\beta = 31.95 \times 10^3$, and $\gamma = 3.00 \times 10^3$ (see Fig. 1(a)). All results of this study are obtained by assuming this non-monotonic radial electric field that is seen as a factor to develop a particle transport barrier that allows trapping chaotic trajectories inside the plasma.[13] For monotonic safety factor profile, we use $q(I) = 2.00 + 3.00\,I^2$ and for non-monotonic one $q(I) = 5.00 - 6.30\,I^2 + 6.30\,I^3$, see Fig. 1(b). These profiles are chosen to investigate the influence of

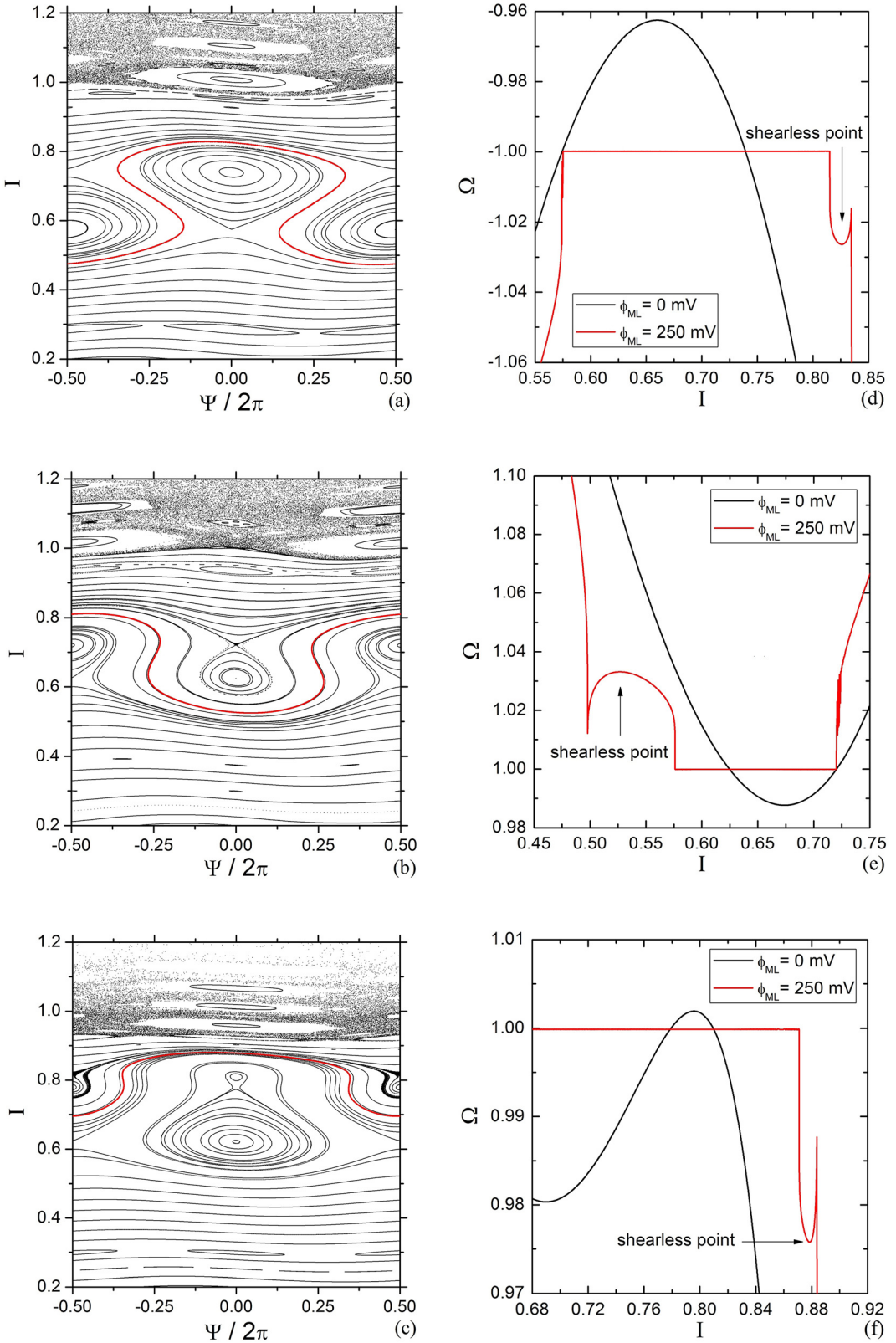

FIG. 4. Poincaré maps for potential mode amplitude $\phi_{ML} = 250\,mV$ and positive uniform velocity (a), negative uniform velocity (b), and sheared velocity (c) profiles showed in Fig. 2. The shearless curves are depicted in red in (a), (b), and (c). For these maps, we used a non-monotonic safety factor profile showed in Fig. 1(b). Rotation number profiles at $\Psi/2\pi = 0$ for positive uniform velocity (d), negative uniform velocity (e), and sheared velocity (f).

magnetic and electric shears, combined to the particle parallel velocity, on the particle transport.

The simulations are performed using the particle parallel velocities $v_{\parallel} = 2.5\,\mathrm{km/s}$, $v_{\parallel} = -2.5\,\mathrm{km/s}$, and $v_{\parallel}(I) = 2.5\tanh(10.0\,I - 9.6)\,[\mathrm{km/s}]$ in the case of sheared profile characterized by gradients at the plasma edge (see Fig. 2). These velocity profiles are compatible with the experimental measurements in TCABR tokamak.[19] The lowest angular frequency in the power spectrum obtained by floating potential measurements is $\omega_0 = 6 \times 10^4\,\mathrm{rad/s}$. Finally, for this tokamak configuration, we use $R = 61\,\mathrm{cm}$, $a = 18\,\mathrm{cm}$, and $B = 1.1\,T$.[12,13,19] Despite using TCABR parameters in this work, this methodology can be explored in different tokamaks to investigate turbulent transport in tokamaks edge.

IV. PARALLEL VELOCITY EFFECTS WITH MONOTONIC SAFETY FACTOR PROFILE

Initially, we investigate the particle trajectories for each of the three parallel velocity profiles, shown in Fig. 2, with the electric field profile of Fig. 1(a) and the monotonic safety factor profile of Fig. 1(b). For each velocity profile, we present a set of orbits in the phase space and the rotation number profiles, calculated as defined in Section III, i.e., for orbits starting with a fixed initial helical angle Ψ in the phase space. The periodic orbits are observed around the radial position where the rotation number assumes rational values and the shearless radial position is located at the maximum or minimum of the rotational number profiles.

Figure 3 shows Poincaré sections of the drift map for $\phi_{ML} = 250\,\mathrm{mV}$ using three different velocity profiles. For positive uniform velocity profile, we observe resonance condition around $I = 0.5$ and chaotic particle trajectories occur for $I > 0.8$, as shown in Fig. 3(a). Changing $v_{\parallel}$ for a negative uniform velocity, we observe the positions of hyperbolic points replaced by stable elliptic points, as seen in Fig. 3(b). The Poincaré map for sheared velocity profile is shown in Fig. 3(c), where we observe the inner island as the one around $I = 0.5$ seen in Fig. 3(b). However, we observe the periodic structures embedded in a chaotic sea with the elliptic points located at $\Psi/2\pi \approx 0$ as those seen in Fig. 3(a).

We present in Figs. 3(d)–3(f) the rotation number profiles according to Figs. 3(a)–3(c), respectively. For comparisons, the rotation number profiles are calculated not only for

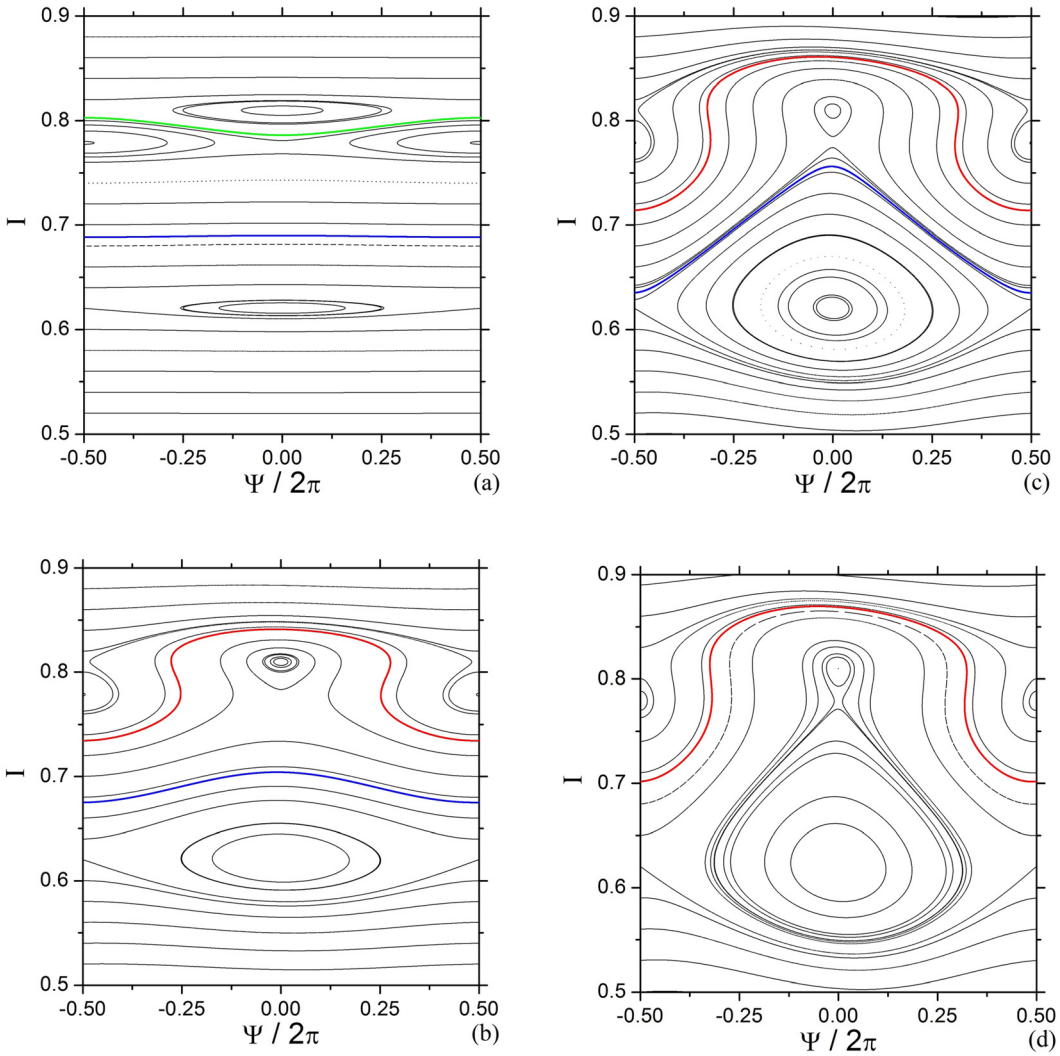

FIG. 5. Poincaré maps for potential mode amplitudes $\phi_{ML} = 1\,mV$ (a), $\phi_{ML} = 20\,mV$ (b), $\phi_{ML} = 65\,mV$ (c), and $\phi_{ML} = 100\,mV$ (d) for sheared velocity profile showed in Fig. 2. The shearless curves are depicted as the same color of those showed for the sheared points in Fig. 6. For these maps, we used a non-monotonic safety factor profile showed in Fig. 1(b).

$\phi_{ML} = 250\,\text{mV}$, the perturbing wave amplitude value used to obtain the phase space, but also for $\phi_{ML} = 0$, assuming initial conditions at $\Psi/2\pi = 0$.

In Fig. 3(d), we obtain negative values for rotation number due to the changes $\Delta\Psi$ from positive to negative values. Thus, altering the signal of $v_{\parallel}$, we modify the helicity variation. Note in Fig. 3(a) the island around $I = 0.5$, which corresponds to a resonance condition with null global rotation number. The changing of $v_{\parallel}$ signal in Fig. 3(e) leads to the replacement from elliptic point to a hyperbolic one, located around $I = 0.5$. In Fig. 3(f), we indicate the coordinate for which $d\Omega/dI \approx 0$, position correspondent to the shearless curve depicted in red for the mapping of Fig. 3(c). Therefore, the maximum value of the numerically obtained rotation number profile for sheared velocity is observed at $I \approx 0.86$ in Fig. 3(f). With this observation, we determine, for an initial condition ($I = 0.86$, $\Psi/2\pi = 0$), the shearless curve in the map of Fig. 3(c), i.e., the location of the barrier is identified by the shearless point of the rotation number profile.

V. PARALLEL VELOCITY EFFECTS WITH NON-MONOTONIC SAFETY FACTOR PROFILE

In addition to Sec. IV, we investigate the parallel velocity effects over the particle transport when assuming the non-monotonic safety factor profile, showed in Fig. 1(b). For positive uniform velocity profile, we observe in Fig. 4(a) a double resonance, with twin islands located at $I \approx 0.7$ and chaotic particle trajectories for $I > 0.9$. As observed in Sec. IV, the change to the negative uniform velocity profile shifts the position of elliptic to the hyperbolic points, as seen in Fig. 4(b). In case of sheared parallel velocity profile, we obtain a mapping characterized by both radial regions of Figs. 4(a) and 4(b), for low and high I values, but with an evidence of a saddle-node bifurcation, as seen in Fig. 4(c).

The periodic structures observed in these mappings can be explained by the rotation number profiles Ω, showed in Figs. 4(d)–4(f). From these profiles, we observe twin islands caused by a resonance with rational number of Ω. By comparing the position of the shearless line with the twin islands in Figs. 4(a) and 4(b), we recognize the occurrence of a bifurcation involving the island reconnection.[22] In Fig. 4(c), we observe a resonance that leads to a different topology, not observed in Figs. 4(a) and 4(b), discussed later on.

The map for sheared velocity and non-monotonic safety factor profile is now further studied to show the influence of mode amplitude on the shearless bifurcations. In Fig. 5, we present mappings and colored shearless invariant curves obtained for sheared velocity using the following mode amplitudes: 1 mV, 20 mV, 65 mV, and 100 mV. Figures 5(a)–5(c) have two shearless curves, while Fig. 5(d) has only one. Figures 6(b)–6(e) show the corresponding rotation number profiles with the shearless points indicated by the same color used to represent the shearless curves in Fig. 5. Note that, for comparison, Fig. 6(a) shows the rotation number profile for null mode amplitude with two shearless points due to the non-monotonic equilibrium profile (as expected from $R_1(I)$ expression given by Eq. (5)).

As the amplitude mode increases the twin islands show a saddle-node bifurcation, in which the two shearless curve positions are displaced from the initial radial positions seen for low amplitudes. Thus, in Fig. 5(a), even for the low amplitude $\phi_{ML} = 1\,\text{mV}$, we observe the twin islands. Increasing the amplitude to $\phi_{ML} = 20\,\text{mV}$, the twin islands about $I \approx 0.8$ go through a reconnection, as showed in Fig. 5(b). The two shearless curves approach each other as the perturbation parameter increases further, as seen in Fig. 5(c) for $\phi_{ML} = 65\,\text{mV}$. The twin islands also approach to the inner island, originating a saddle-node bifurcation, where the elliptic points are aligned and sharing the same periodic structure for $\phi_{ML} = 100\,\text{mV}$, as seen in Fig. 5(d). Furthermore, only one shearless curve survives such bifurcation. The displacement of the shearless curves and the bifurcations, with the increase of potential mode amplitude, is confirmed by the maximum and minimum of rotational number profiles showed in Figs. 6(b)–6(e).

Finally, increasing further the perturbation for $\phi_{ML} = 300\,\text{mV}$, part of the invariant curves are destroyed and the saddle-node bifurcation is surrounded by chaotic trajectories, as shown in Fig. 7(a). Nevertheless, the shearless curve still survives as confirmed by the rotational number profile, obtained for initial conditions with $\Psi/2\pi = -0.5$, shown in Fig. 7(b).

Complementary, the drift map has also been obtained to investigate how the particle transport becomes significant with the potential mode amplitude increase. Here, we use a color scale relative to the particle initial position to evaluate how the particle transport changes with the potential

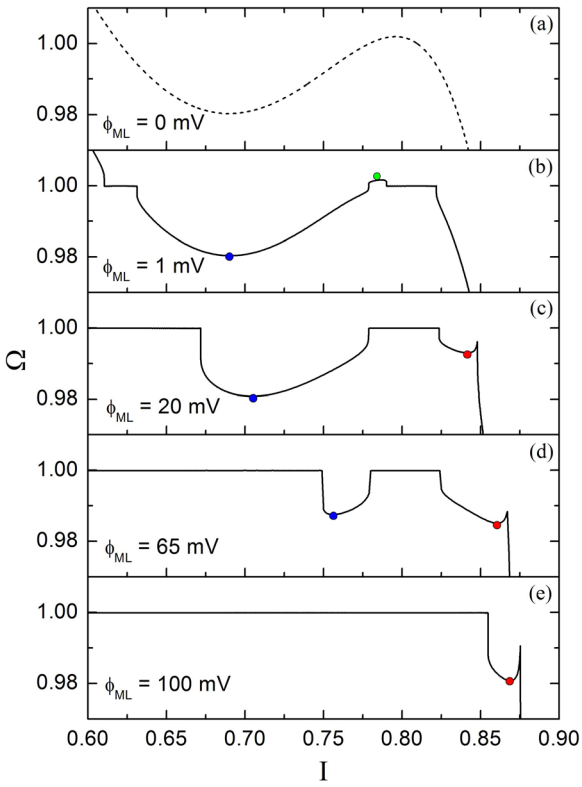

FIG. 6. Rotation number profiles at $\Psi/2\pi = 0$ for the set of maps showed in Fig. 5. The sheared points are depicted using the same colors of those for the shearless curves in Fig. 5.

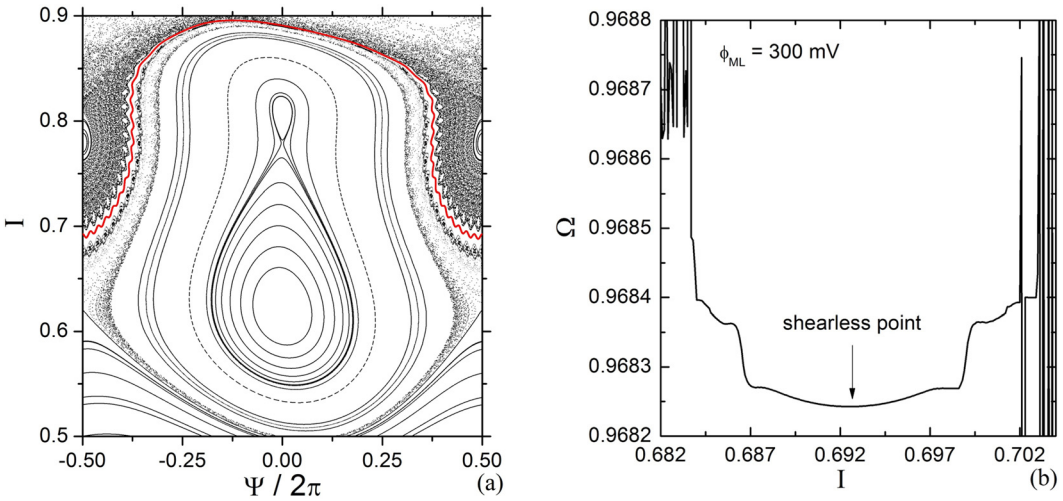

FIG. 7. Poincaré map for potential mode amplitude $\phi_{ML} = 300\,mV$ using non-monotonic safety factor profile of Fig. 1(b) and sheared velocity of Fig. 2. The shearless curve is depicted in red in (a). Rotation number profile (b) for $\Psi/2\pi = -0.5$ for the same parameters of (a).

amplitude. Thus, Fig. 8 shows examples of the mappings, for four different potential amplitudes, having the same initial radial positions indicated by the color scale. As a consequence of the potential amplitude dependence, the same initial colored points are more spread in the phase space for higher amplitudes, as we recognize in Figs. 8(a)–8(d).

In Fig. 8(a), for a low perturbation, $\phi_{ML} = 1$ mV, only a negligible localized transport is noticed. In Fig. 8(b), radial

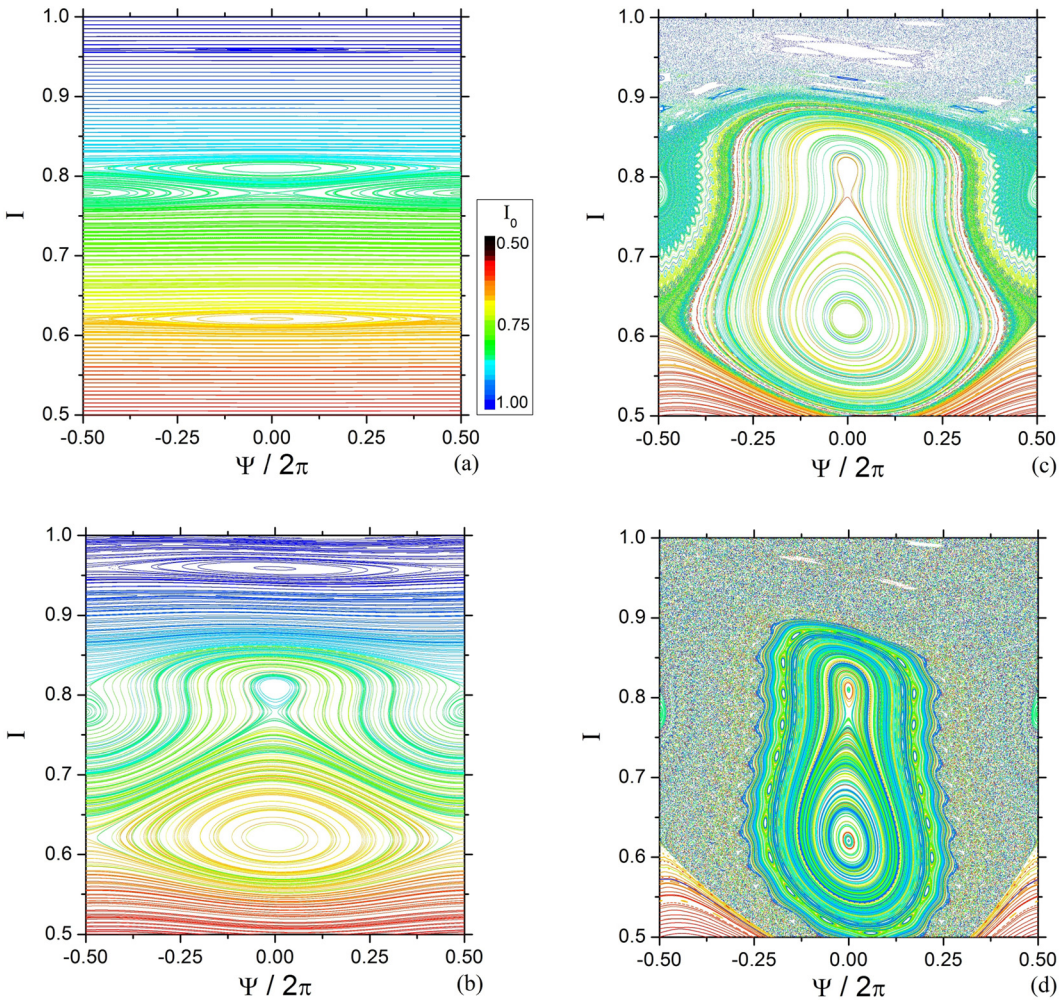

FIG. 8. Symplectic maps for sheared velocity profile of Fig. 2 and potential mode amplitudes $\phi_{ML} = 1\,mV$ (a), $\phi_{ML} = 65\,mV$ (b), $\phi_{ML} = 300\,mV$ (c), and $\phi_{ML} = 500\,mV$ (d). The color scale in these maps indicates the initial radial particle positions showed in (a).

particle displacement is still negligible, but the invariant curves are deformed as the potential mode amplitude is increased to $\phi_{ML} = 65\,\mathrm{mV}$, i.e., the trajectories fill radial positions far away from those observed in Fig. 8(a). On the other hand, the trajectories are chaotically spread at the plasma edge for $\phi_{ML} = 300\,\mathrm{mV}$, as seen in Fig. 8(c). In Fig. 8(d), we observe chaotic trajectories around the saddle-node bifurcation with particle trajectories much displaced from initial positions. These results show long radial particle displacements for several initial conditions, moving to long distance radial positions for which the velocity changes due to the considered velocity radial profile (see Fig. 2). Therefore, these maps allow understanding how the chaos and radial particle displacement develop as the amplitude mode increases at the plasma edge.

VI. CONCLUSIONS

A symplectic drift map was used to describe the particle drift driven by electrostatic wave fluctuations in a velocity shear layer at the tokamak plasma edge considering a large aspect ratio approximation with $E \times B$ flow. We showed that the particle transport at the tokamak plasma edge is much affected by the parallel particle toroidal velocity profile.

With this procedure, we obtained test particle trajectories for chosen safety factor, electric field, and velocity profiles. At the plasma edge, the trajectories are mainly determined by the safety factor and velocity profiles and are identified as regular or chaotic. The chaotic trajectories, associated with the chaotic transport, changed with the velocity profile. For both monotonic and non monotonic magnetic configurations, we observed robust shearless barriers, provided by the gradient velocity layer, separating trajectories in the phase space. We also observe how resonance and shearless curve bifurcations affect the particle transport.

ACKNOWLEDGMENTS

The authors thank the financial support from São Paulo Research Foundation (FAPESP, Brazil) under Grant Nos. 2013/0340-6, 2015/16471-8, and 2011/19296-1, CNPq (Brazil) and CAPES (Brazil) and would like to thank Caroline Gameiro Lopes Martins for helpful discussions.

[1]W. Horton, Rev. Mod. Phys. **71**, 735 (1999).
[2]P. W. Terry, Rev. Mod. Phys. **72**, 109 (2000).
[3]C. P. Ritz, R. D. Bengtson, S. J. Levinson, and E. J. Powers, Phys. Fluids **27**, 2956 (1984).
[4]C. P. Ritz, H. Lin, T. L. Rhodes, and J. A. Wootton, Phys. Rev. Lett. **65**, 2543 (1990).
[5]K. H. Burrell, Phys. Plasmas **4**, 1499 (1997).
[6]W. Horton, *Turbulent Transport in Magnetized Plasmas* (World Scientific Publishing Company, Singapore, 2012).
[7]G. V. Oost, J. Adámek, V. Antoni, P. Balan, J. A. Boedo, P. Devynck, I. Ďuran, L. Eliseev, J. P. Gunn, M. Hron, C. Ionita, S. Jachmich, G. S. Kirnev, E. Martines, A. Melnikov, R. Schrittwieser, C. Silva, J. Stöckel, M. Tendler, C. Varandas, M. V. Schoor, V. Vershkov, and R. R. Weynants, Plasma Phys. Controlled Fusion **45**, 621 (2003).
[8]C. Hidalgo, M. A. Pedrosa, and B. Gonçalves, New J. Phys. **4**, 51 (2002).
[9]G. F. Matthews, Plasma Phys. Controlled Fusion **36**, 1595 (1994).
[10]H.-B. Park, E.-G. Heo, W. Horton, and D.-I. Choi, Phys. Plasmas **4**, 3273 (1997).
[11]W. Horton, H.-B. Park, J.-M. Kwon, D. Strozzi, P. J. Morrison, and D.-I. Choi, Phys. Plasmas **5**, 3910 (1998).
[12]F. A. Marcus, I. L. Caldas, Z. O. Guimarães-Filho, P. J. Morrison, W. Horton, Y. K. Kuznetsov, and I. C. Nascimento, Phys. Plasmas **15**, 112304 (2008).
[13]K. C. Rosalem, M. Roberto, and I. L. Caldas, Nucl. Fusion **54**, 064001 (2014).
[14]S. S. Abdullaev, A. Wingen, and K. H. Spatschek, Phys. Plasmas **13**, 042509 (2006).
[15]P. J. Catto, M. N. Rosenbluth, and C. S. Liu, Phys. Fluids **16**, 1719 (1973).
[16]D. R. McCarthy, J. F. Drake, and P. N. Guzdar, Phys. Fluids B **5**, 2145 (1993).
[17]W. Horton, Plasma Phys. Controlled Fusion **27**, 937 (1985).
[18]J.-M. Kwon, W. Horton, P. Zhu, P. J. Morrison, H.-B. Park, and D.-I. Choi, Phys. Plasmas **7**, 1169 (2000).
[19]J. H. F. Severo, I. C. Nascimento, V. S. Tsypin, and R. M. O. Galvão, Nucl. Fusion **43**, 1047 (2003).
[20]C. G. L. Martins, E. R. de Carvalho, I. L. Caldas, and M. Roberto, J. Phys. A: Math. Theor. **44**, 045102 (2011).
[21]I. L. Caldas, R. L. Viana, C. V. Abud, J. C. D. Fonseca, Z. O. Guimarães-Filho, T. Kroetz, F. A. Marcus, A. B. Schelin, J. D. Szezech, Jr., D. L. Toufen, S. Benkadda, S. R. Lopes, P. J. Morrison, M. Roberto, K. Gentle, Y. Kuznetsov, and I. C. Nascimento, Plasma Phys. Controlled Fusion **54**, 124035 (2012).
[22]D. del-Castillo-Negrete, J. M. Greene, and P. J. Morrison, Physica D **91**, 1 (1996).